Table of contents:

Supplementary Figure 33. Relationship between the sweat induction location/method and sweat pH.

Supplementary Figure 34. Operation of battery-aided wearable device for over 24 hours while exposed to various illumination conditions.

Supplementary Figure 35. Evaluation of the light-powered wearable device for physiological monitoring during sleep without the access to light.

Supplementary Table 1. FPSC performance under full sunlight conditions.
Supplementary Table 2. FPSC performance under LED illumination.
Supplementary Table 3. List of the best performing indoor flexible solar cells among different PV technologies.
Supplementary Table 4. Performance of quasi-2D FPSC under laser illumination.
Supplementary Table 5. Average power consumption of electronic system supplied at 3 V while performing various operations under varying operation parameters.

Supplementary Video 1. Demonstration of the wearable sensor mobile application
Supplementary Video 2. Light powered iontophoresis-based prolonged microfluidic sweat sampling and sweat rate monitoring at rest.

Supplementary Note 1. Design and considerations of monochromatic light source PCE measurement approach for indoor and low light PV.

Solar cells behave considerably different under high and low light illumination conditions, with the major change emerging form R_p, R_s, and charge carrier concentration[1,2]. Solar cells under low light illuminations perform better with increasing R_p (higher R_p correlates with increased FF and V_{oc}). On the other hand, R_s, which greatly influences the device performance under AM1.5G conditions (higher R_s leads to decrease in FF and J_{sc}), tends to have little effect on low light device performance. Additionally, fewer incoming photons under low light illumination as well as good spectral matching of the indoor light source to the spectral response characteristics of perovskite solar cells result in less recombination and thus contribute to increase in performance.

Since incoming light is determined by the environmental conditions and J_{sc} scales linearly with the light intensity, the behavior of V_{oc} and FF become the deciding factor that determine solar cell low light performance. V_{oc} decreases as a function of decreasing light intensity, with the rate of decrease becoming stronger after a certain critical illuminance. On the other hand, FF increases as the light intensity decreases and then starts to decrease also after certain critical illuminance is reached. Thus keeping both V_{oc} and FF high (through trap passivation and judicious perovskite composition engineering) as light intensity decreases is the key to achieving high efficiency under low light illumination[3].

Shockley-Queisser PCE limit of a solar cell with an optimal bandgap (1.82–1.96 eV) under indoor illuminance levels (100-1000 lx) using a common LED light source has been calculated to be between 51 and 57 %, which is considerably higher than that of the corresponding 33 % at 1 Sun AM1.5G irradiation [4]. Nevertheless, a consensus on standardized PCE measurement conditions, like the well-established outdoor PV method, is yet to emerge[5]. As a result, several different light sources, illuminance levels, measurement set-ups, and protocols have been reported in literature which can have a noticeable effect on PCE even when measured on the same device under the same illuminance[6].

Therefore, in this study we use monochromatic (laser) measurement, as a complementary technique that offers a unique way to assess PCE value of our quasi-2D FPSC, independent of the light source. It presents a so-called "best-case scenario" performance of a given device, with reduced influence of sub-bandgap and relaxation losses. For this purpose, a laser wavelength (λ = 637 nm) was chosen to be sufficiently close to the spectral response cut-off and have sufficiently high EQE

in that region of measurement. Additionally, measuring the cell performance over a range of irradiances reveals the incident power range, where the device is best at converting light into electricity, while also bringing forward insights about device physics based on the trends of cell parameters (V_{oc}, J_{sc}, FF) as the function of light intensity. Nevertheless, the calculated values need to be used with caution and consideration, when trying to extrapolate them to real world situations, where either one or multiple light sources with various spectral shapes and intensities illuminate the device.

Supplementary Note 2. Optimization and characterization of electronic system power consumption

The wearable device can perform various operations including but not limited to current-monitored iontophoresis, potentiometry, amperometry, voltammetry, impedance analysis, multiplexed measurements (up to four voltage/current measurement channels), and on-body measurement sequences (multiplexed measurements with periodic impedance measurements). In a typical workflow, the programmable system-on-chip (PSoC) Bluetooth low energy (BLE) module acts as a data bridge between the electrochemical analog front-end (AFE) and a host software (mobile phone or PC), wherein it encodes and writes measurement instructions to the electrochemical AFE, then decodes and transmits the AFE's measurement data to a host software via BLE (**Supplementary Fig. S13c**). The electrochemical AFE, on the other hand, sequentially performs tasks as instructed by the PSoC BLE module and saves all measurement data in its internal memory, while periodically interrupting the PSoC BLE module to fetch the saved measurement data. Firmware can be optimized to balance tradeoffs between measurement intervals and overall power consumption.

The power output of the solar cell can vary as the lighting conditions change, and while it is possible to maximize the electrochemical measurement, data processing, and wireless communication intervals (~ 30 s, ~ 300 s, and ~ 300 s respectively) such that the wearable device can always operate at its lowest possible power consumption mode, a higher sampling and data transmission rate improves data continuity and user experience. Therefore, the wearable device dynamically adapts the operation parameters such that it can sample, process, and transmit data as frequently as the solar cell power output permits.

To accurately configure the operation parameters, it is necessary to be able to calculate the power consumption of the system based on the operation parameters. Each operation consists of the combination of several passive tasks (hibernate, sleep, and iontophoresis) and active tasks (measurement, process, and BLE). During hibernation, most blocks of the electronic system are inactive; during sleep, most blocks of the electronic system are inactive except the low power potentiostat loop; and during iontophoresis, most blocks of the electronic system are inactive except the iontophoresis block and the low power potentiostat loop. During a measurement task, the electrochemical AFE performs an analog-to-digital conversion (ADC) measurement; during a processing task, the AFE performs an ADC measurement and then the PSoC BLE module fetches

varying amounts of ADC measurement data stored in the AFE's internal memory and processes them; during a BLE task, varying amounts of processed data can be transmitted as BLE indications (BLE connection) or as BLE advertisements (no BLE connection). Each of these tasks consumes different amounts of power. In addition, due to the dynamic conversion efficiency of the voltage regulator and boost converter, the power consumption of the system varies depending on the voltage level supplied by the energy storage capacitor. The power/energy consumption of each task when powered at varying supply voltages is shown in **Supplementary Fig. 15**.

For each operation, we varied the operation parameters and measured the average power consumption when supplied at 3 V. **Supplementary Fig. 16** displays the power consumption profiles for various operations performed at varying operation parameters measured over a 20 s timespan. Most power consumption profiles were collected at a sampling rate of 10 kHz, but the power consumption profile for iontophoresis was collected at a sampling rate of 1 kHz because the transient spikes in power consumption caused by the boost converter for iontophoresis would obscure the plot visually at high sampling rates. However, sampling rates from 1 kHz to 100 kHz all yielded accurate values for average power consumption. Furthermore, **Supplementary Fig. 22** shows expanded (10 min) power consumption profiles of on-body measurement sequences that were used for in vitro validation flow tests and on-body experiments shown in **Fig. 3f**. **Supplementary Table 4** shows the average power consumption of all operations performed at varying operation parameters. Operation parameters chosen for use during experiments are highlighted in yellow and green.

Supplementary Note 3. Design considerations and optimization of microfluidic sweat processing system

The design goal for the microfluidic sweat processing system was to develop a system that can induce and extract the sweat for prolonged durations above a minimal threshold flow rate while consuming minimal amounts of power. Trade-offs between power consumption for iontophoresis and the size of the carbagels, geometric location and orientation of the gels with respect to the sweat accumulation reservoir, and distance between the gels and sweat accumulation reservoir were considered. The power consumption of the iontophoresis circuit is positively correlated to the total current applied and the compliance voltage of the constant current source. As iontophoretic current density is positively correlated with regional sweat rate, power consumption could be minimized by minimizing the area of the carbagel. On the other hand, while carbachol can stimulate neighboring sweat glands, if the carbagel is too small, the sweat gland density around the gel can be low, generating low sweat volume. The next factor considered was the orientation of the gels with respect to the sweat accumulation reservoir. We found that locating the sweat accumulation reservoir between the anode and cathode can maximize extraction efficiency as the majority of the drug is delivered across the anode and cathode. Another factor considered was the distance between the gels. If the anode and cathode are too close, the drug delivery area may be too small and it is possible that not enough sweat glands are activated. However, increasing the inter-gel distance above a certain extent does not increase sweat gland activation and only increases the impedance between the two carbagels, which necessitates a higher compliance voltage and power consumption for the iontophoresis circuit. Regarding the distance between the carbagels and the sweat accumulation reservoir, sweat extraction improved when the sweat accumulation reservoir was closer to the anodic carbagel (where the drug is loaded). However, if the distance between the gel and accumulation reservoir was closer than 1 mm, the adhesive would have difficulty maintaining the sweat within the sweat accumulation reservoir and sweat would leak at times. With all these considerations in mind, our final carbagel area was 15 mm^2 per electrode, distance between the carbagels was 4 mm, and the distance between the carbagel and the sweat accumulation reservoir was 1.2 mm. A current of 55 μA was delivered for iontophoretic stimulation as lower currents did not result in sufficient sweat output, and higher currents lead to an increased power consumption and did not necessarily result in a longer stimulation duration.

The final microfluidic sweat processing system consists of three main layers, the sweat accumulation layer, the channel layer, and the reservoir layer (**Supplementary Fig. 1**). All layers of the microfluidic system contain two large cutouts for holding the carbagels. In addition to these cutouts, the accumulation layer (0.13 mm) contains a well (same dimensions as the sensor reservoir) for sweat accumulation; the channel layer (0.64 mm) contains a sweat rate channel (36 μL or 95 μL capacity) for processing high volumes of sweat and a counter electrode-shaped inlet to transport the accumulated sweat into the sensor reservoir; and the reservoir layer (0.13 mm) contains a compact sensor reservoir (1.1 μL capacity) to enable rapid refreshing of sweat and a microfluidic channel to flush out the sweat through the sweat rate channel.

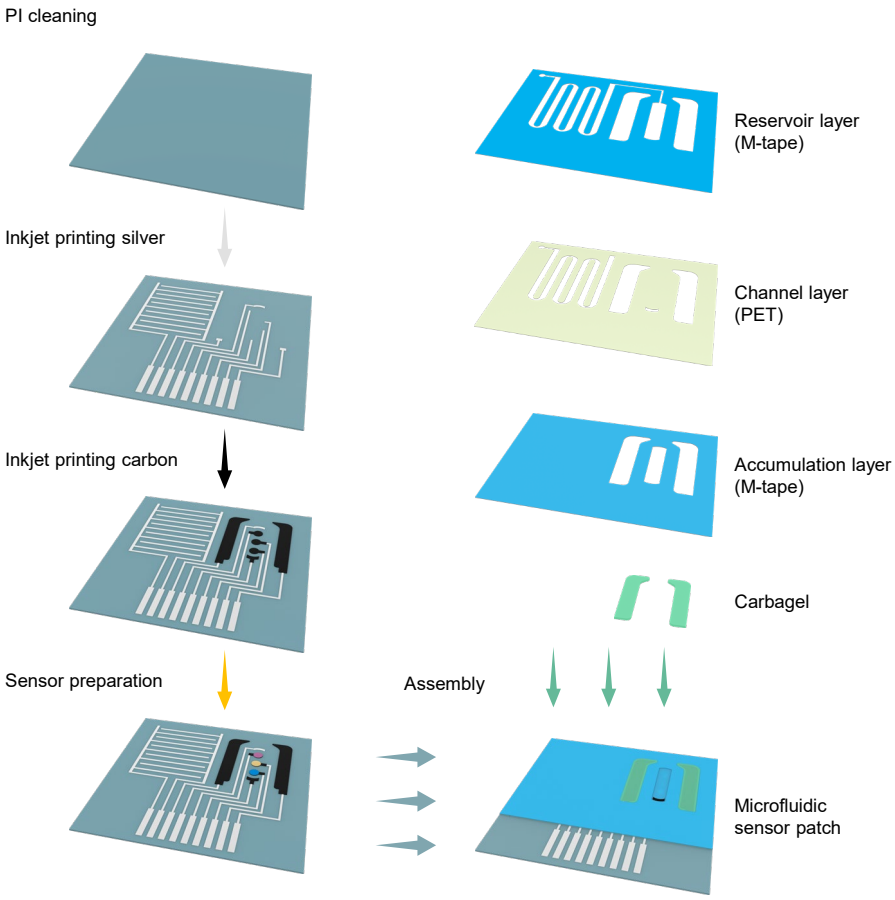

Supplementary Figure 1. Schematic depicting the fabrication process of the microfluidic sensor patch. For the preparation of sensors, the PI substrate was cleaned *via* O_2 plasma surface treatment, followed by the sequential inkjet printing of silver and carbon electrodes, which were further modified for electrochemical detection. The microfluidic layers consisting of medical tapes and PET films were patterned using a CO_2 laser cutter, then assembled onto the sensor patch along with the carbagels.

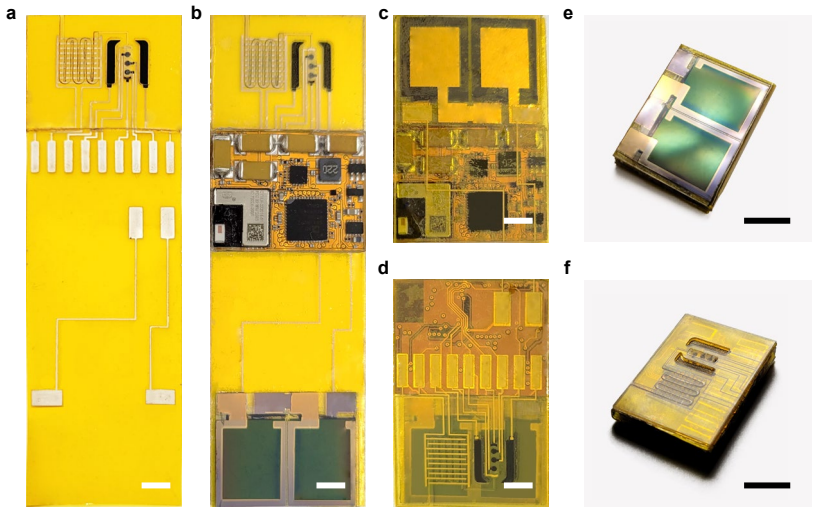

Supplementary Figure 2. Photos showing the assembly process of the wearable device. a–d, The FPSC, electronics, and microfluidic sensor patch are assembled in an origami style. Scale bars, 5 mm. **e,f,** The top view of the fully assembled wearable device with the solar cell facing up (**e**), and the bottom view of the fully assembled wearable device with the microfluidic sensor patch facing up (**f**). Scale bars, 1 cm.

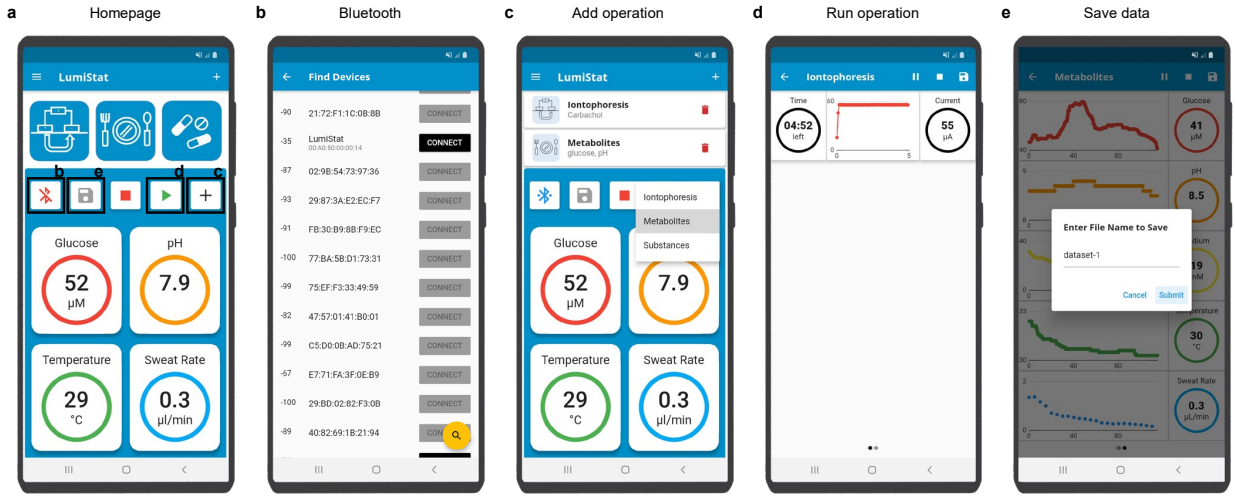

Supplementary Figure 3. Operation manual for the solar cell-powered wearable sweat analysis mobile application. a, Homepage of the Wearable Sweat Sensor App displaying the most recent sensor readings on a scrollable grid view. **b–e**, Above the sensor readings, there is a list of command buttons such that the app can connect to the wearable device over BLE (**b**), serially add operation sequences (e.g., iontophoretic sweat stimulation and multimodal metabolite monitoring) (**c**), serially run all the added operations and display the real time data (**d**), save acquired data to the phone (**e**), and stop all operations.

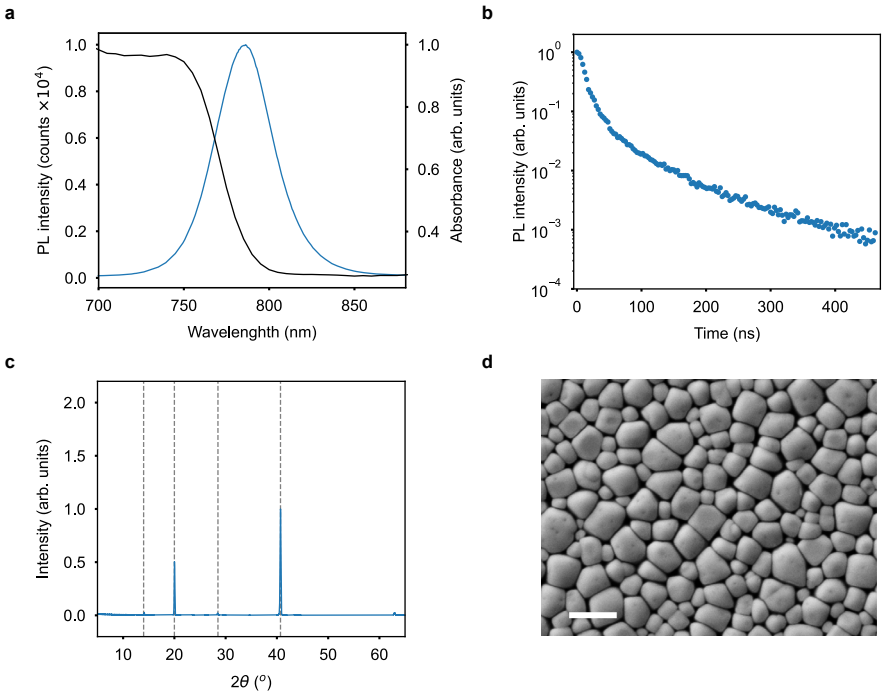

Supplementary Figure 4. Quasi-2D perovskite $(MBA)_2(Cs_{0.12}MA_{0.88})_6Pb_7(I_xCl_{1-x})_{22}$ material characterization. a, Photoluminescence spectrum with the peak at 786 nm and corresponding UV/Vis absorption spectrum. **b,** Transient photoluminescence measurement with triexponential fit ($i = A_1 \exp(-t/\tau_1) + A_2 \exp(-t/\tau_2) + A_3 \exp(-t/\tau_3)$) used to calculate fast (τ_1 = 13 ns), intermediate (τ_2 = 118 ns), and slow (τ_3 = 153 ns) time decay constants. **c,** XRD diffraction pattern showing sharp and narrow peaks at 14°, 20°, 28.5°, and 40.7° corresponding to (100), (112), (220), and (224) planes of tetragonal perovskite structure[7]. **d,** SEM of the perovskite film with individual grains reaching the size of above 1 μm. Scale bar 1, μm. Experiments were repeated five times independently with similar results.

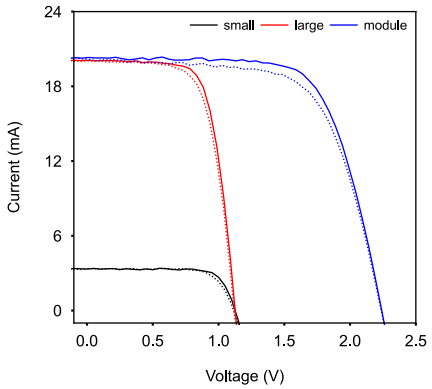

Supplementary Figure 5. Performance of quasi-2D FPSC under simulated sunlight illumination (AM1.5G). Example IV curves of small area (black), large area (red), as well as the module (blue) solar cells, measured in forward (dashed) and reverse (solid) scan directions.

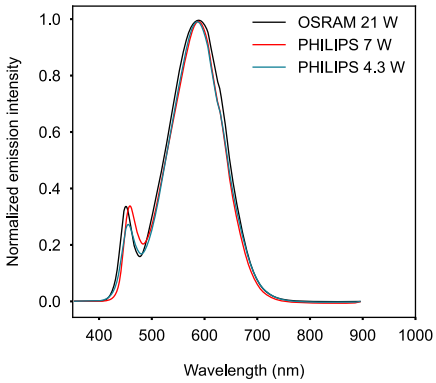

Supplementary Figure 6. The emission spectra of light bulbs used in indoor lighting solar cell performance testing. Room-light LED (2700 K) light bulbs of various brightness used to evaluate the performance of the quasi-2D FPSC over a broad range of illuminance. Osram 21 W (black), Philips 7 W (red), and Philips 4.3 W (red).

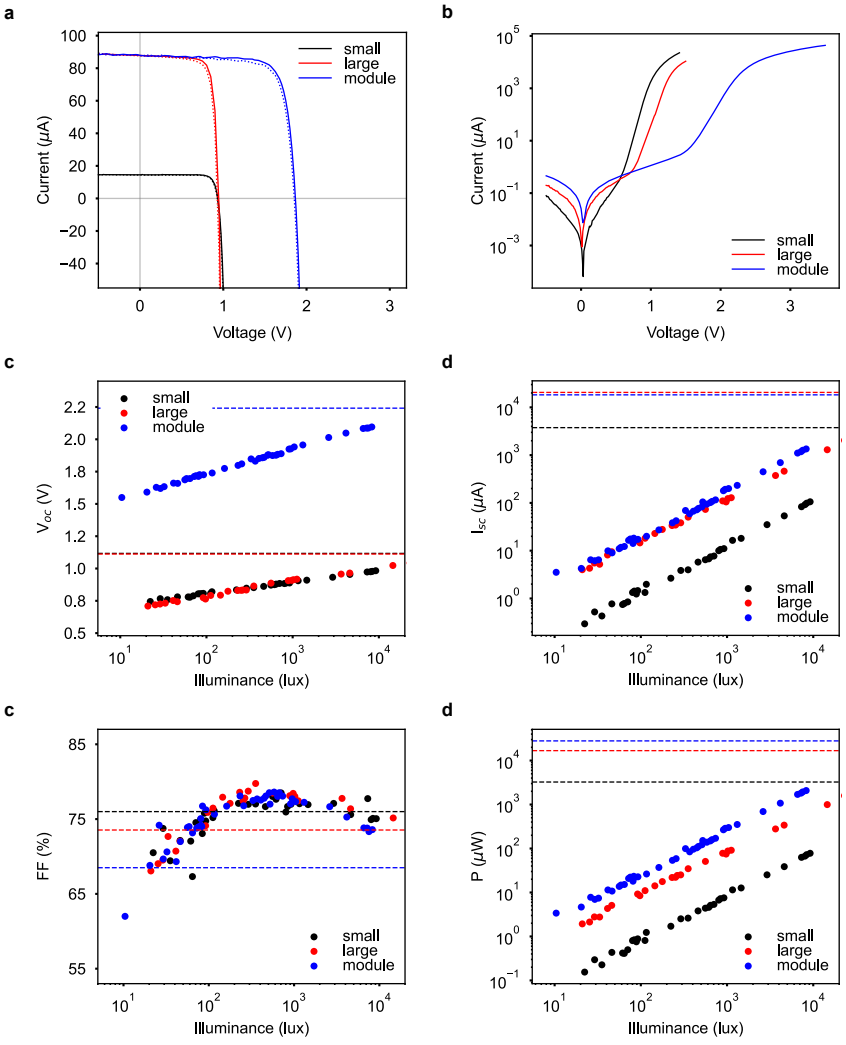

Supplementary Figure 7. Performance of quasi 2D FPSC under indoor lighting. Measurements were performed on devices with small (0.165 cm^2, black), and large (1 cm^2, red) areas as well as modules [2 individual 1 cm^2 cells connected in series] (2 cm^2, blue). **a,** IV curves recorded under indoor 600 lux illumination using a 2700K household LED light bulb. **b,** Dark IV curves of the corresponding devices. **c,** Open circuit voltage as a function of light intensity. Solid lines show the linear fit used for estimation of ideality factor (n) in two regions below (*low*) and above (*high*) 200 lx. For small area devices $n_{high} = 1.50$ and $n_{low} = 1.53$, which suggests an overall superposition of bimolecular and monomolecular (trap-assisted recombination) nonradiative recombination processes in these two regions. Large-area devices have $n_{high} = 1.61$ and $n_{low} = 1.88$, both larger than in their small area counterparts, suggesting higher probability of defects occurring in these devices. Additionally, $n_{low} > n_{low}$ suggests that trap-assisted recombination will be the

limiting the performance in this low light intensity region (<200 lx). Corresponding V_{oc} values measured at AM1.5G are highlighted with a dashed line (V_{oc} (small) = 1.106 V, V_{oc} (large) = 1.109 V, V_{oc} (module) = 2.241 V). **d,** Short circuit current as a function of light intensity, with all three example showing a linear relationship with illuminance. Corresponding I_{sc} values measured at AM1.5G are highlighted with a dashed line (I_{sc} (small) = 3.58 mA, I_{sc} (large) = 20.54 mA, I_{sc} (module) = 18.26 mA). **e,** The plot of fill factor as a function of light intensity. In all three cases the cells show increase in value when compared to AM1.5 conditions. The initial decrease of FF down to 200 lx suggests predominantly bimolecular recombination mechanism, and the following decrease below 200 lx indicates primarily trap-assisted recombination in that illuminance region. Corresponding FF values calculated at AM1.5G are highlighted with a dashed line (FF (small) = 75.02 %, FF (large) = 72.54 %, FF (module) = 68.50 %). **f,** Power density as a function of illuminance. Corresponding values calculated at AM1.5G are highlighted with a dashed line (P (small) = 2.8×10^3 μW, P (large) = 1.7×10^4 μW, P (module) = 2.8×10^4 μW).

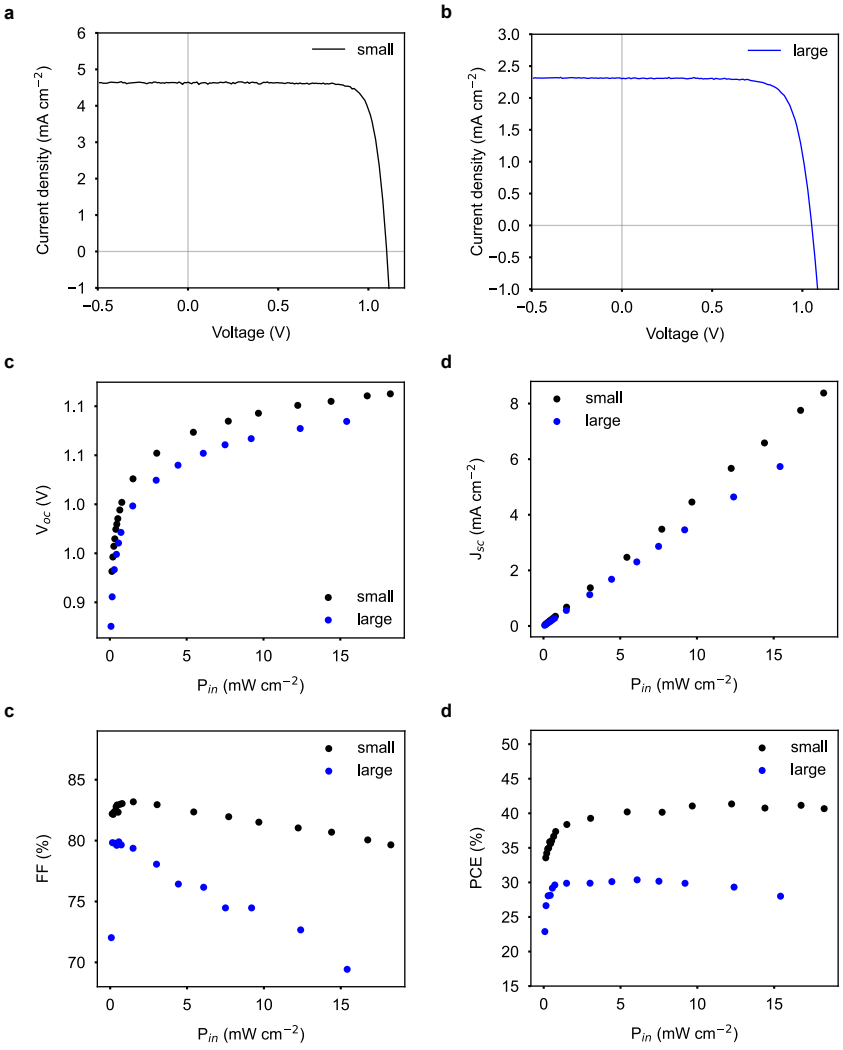

Supplementary Figure 8. Monochromatic (laser) PCE measurement of FPSC in the low light region. a,b, Examples of highest efficiency IV curves measured for small (PCE = 41.3 % at 12.23 mW cm^{-2}, black) (**a**) and large area (PCE = 30.4 % at 5.43 mW cm^{-2}, blue) (**b**) solar cells. **c,** Open circuit voltage as a function of incident power (irradiance). **d,** Short circuit current density of both small and large devices scales up linearly with increasing irradiance. **e,** FF of both types of active area devices increases at different rates up until 1-2 mW cm^{-2}. The sharp decrease in FF at values below 1-2 mW cm^{-2} could be evidence of increasing role of trap-assisted recombination under very low illumination conditions. **f,** PCE as a function of incident power shows a broad region of high performance at low light conditions for both small and large area FPSC.

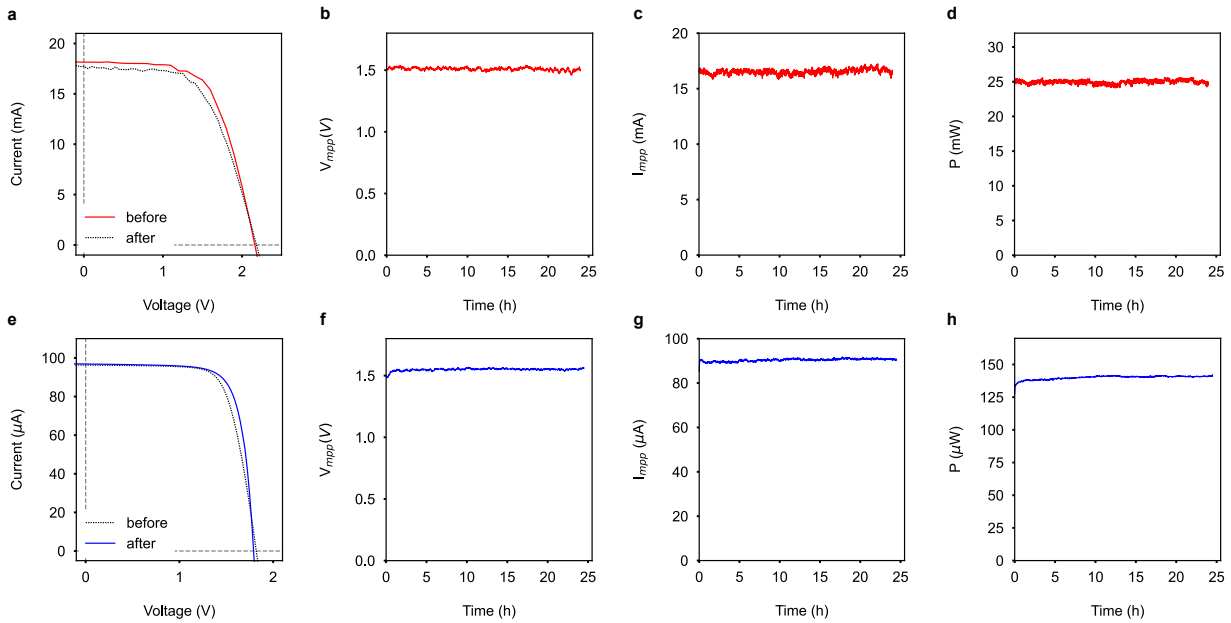

Supplementary Figure 9. Operational stability of quasi-2D FPSC module. a, IV curves before (black) and after (red) maximum power point (MPP) tracking for 24 hour under simulated sunlight (AM1.5). **b-d,** Corresponding maximum power point voltage (V_{mpp}) (**b**), maximum power point current (I_{mpp}) (**c**), and power output (P) (**d**) during the tracking. **e-g,** IV curves V_{mpp} (**e**), I_{mpp} (**f**), and P (**g**) of the same module operating under indoor 600 lx LED room-light illumination conditions for 24 hours.

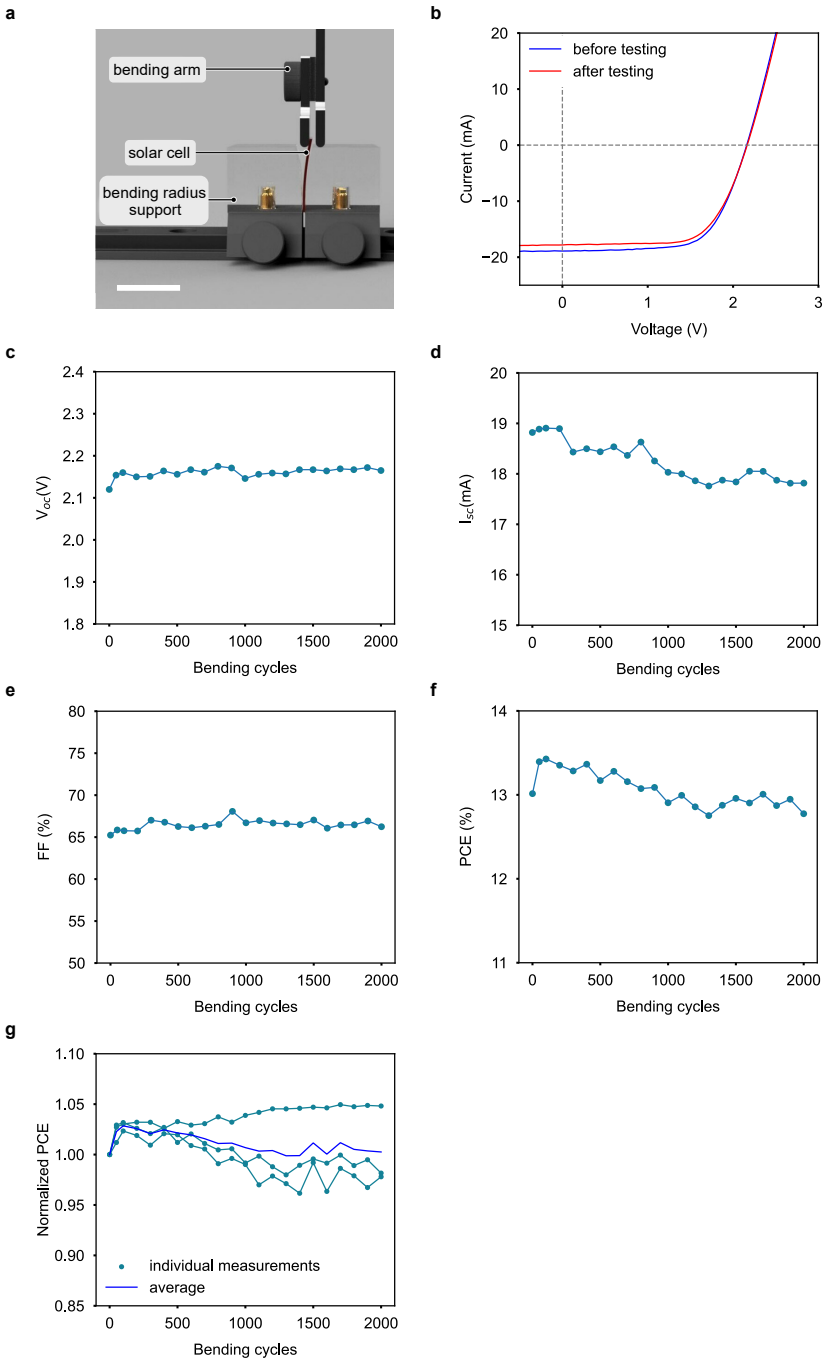

Supplementary Figure 10. Mechanical stability of large FPSC cells. a, Diagram of the setup used to perform mechanical stability test. Scale bar, 1 cm. **b,** JV curves of the large solar cell before and after mechanical testing. **c–f,** Open-circuit voltage (V_{oc}) (**c**), short circuit current density (J_{sc}) (**d**), fill factor (FF) (**e**), and PCE as extracted from measured JV curves (AM1.5) (**f**) during the mechanical test. **g**, Comparison of normalized PCE of several FPSC module bending tests (5 cm bending radius), as well as their average.

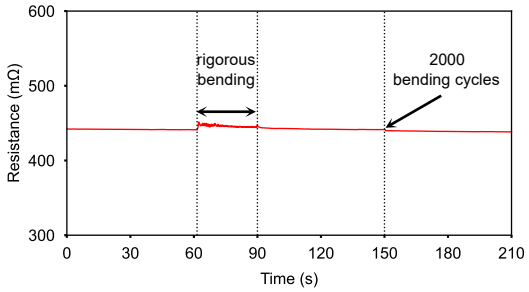

Supplementary Figure 11. Mechanical stability of z-axis conductive tape-based interconnects. Silver interconnects inkjet-printed on a PI substrate were electrically connected to the contact pads of the FPCB v*ia* a z-axis conductive tape. The resistance across the connection was measured before, during, and after rigorous bending, as well as after 2000 controlled bending cycles (bending radius 5 cm).

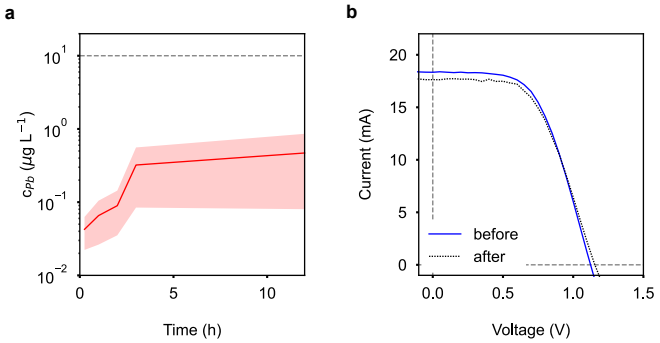

Supplementary Figure 12. Results of FPSC Pb-release tests conducted in deionized water under full sun illumination for intact FPSCs. a, Pb release over a period of 12 hours from a FPSC immersed in DI water under constant AM1.5 illumination. Error band corresponds to confidence interval (n = 9 independent measurements). The gray dashed line highlights the maximum allowable Pb concentration in drinking water as per the Joint FAO/WHO Expert Committee on Food Additives (JECFA). **b,** Corresponding IV curves before and after the DI water Pb-release test, showing no significant change in device performance.

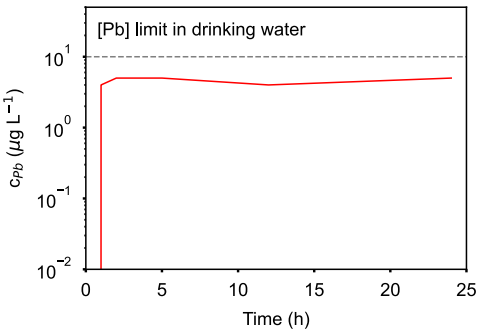

Supplementary Figure 13. Results of Pb leakage tests performed in artificial human sweat solution under full sun illumination for bent FSPCs. The bending test was performed for total 2000 bending cycles under 5 cm bending radius. The gray dashed line highlights the maximum allowable Pb concentration in drinking water as per the Joint FAO/WHO Expert Committee on Food Additives (JECFA).

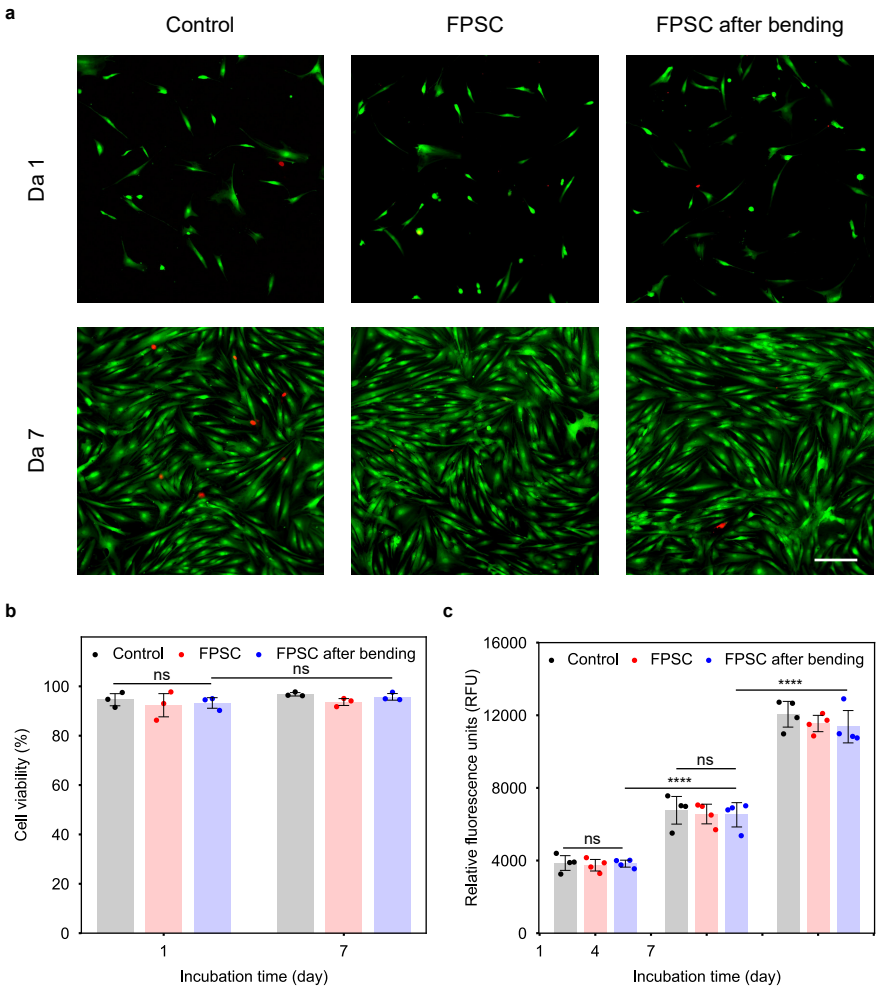

Supplementary Figure 14. Biocompatibility assay on the packaged FPSC. a,b, Fluorescent images (**a**) and bar plot (**b**) of cell viability of human dermal fibroblast (HDF) cells in the presence of FPSC before and after 2000 bending cycles (5 cm bending radius). Scale bar, 200 μm. Data are presented as mean ± SD (n = 3 biologically independent samples). **c,** Bar plot of metabolic activity of human dermal fibroblast (HDF) cells in the presence of FPSC before and after 2000 bending cycles (5 cm bending radius). Data are analyzed using a two-way ANOVA test (Tukey's multiple comparisons) and are presented as mean ± SD (****$p < 0.0001$, n = 4 biologically independent samples).

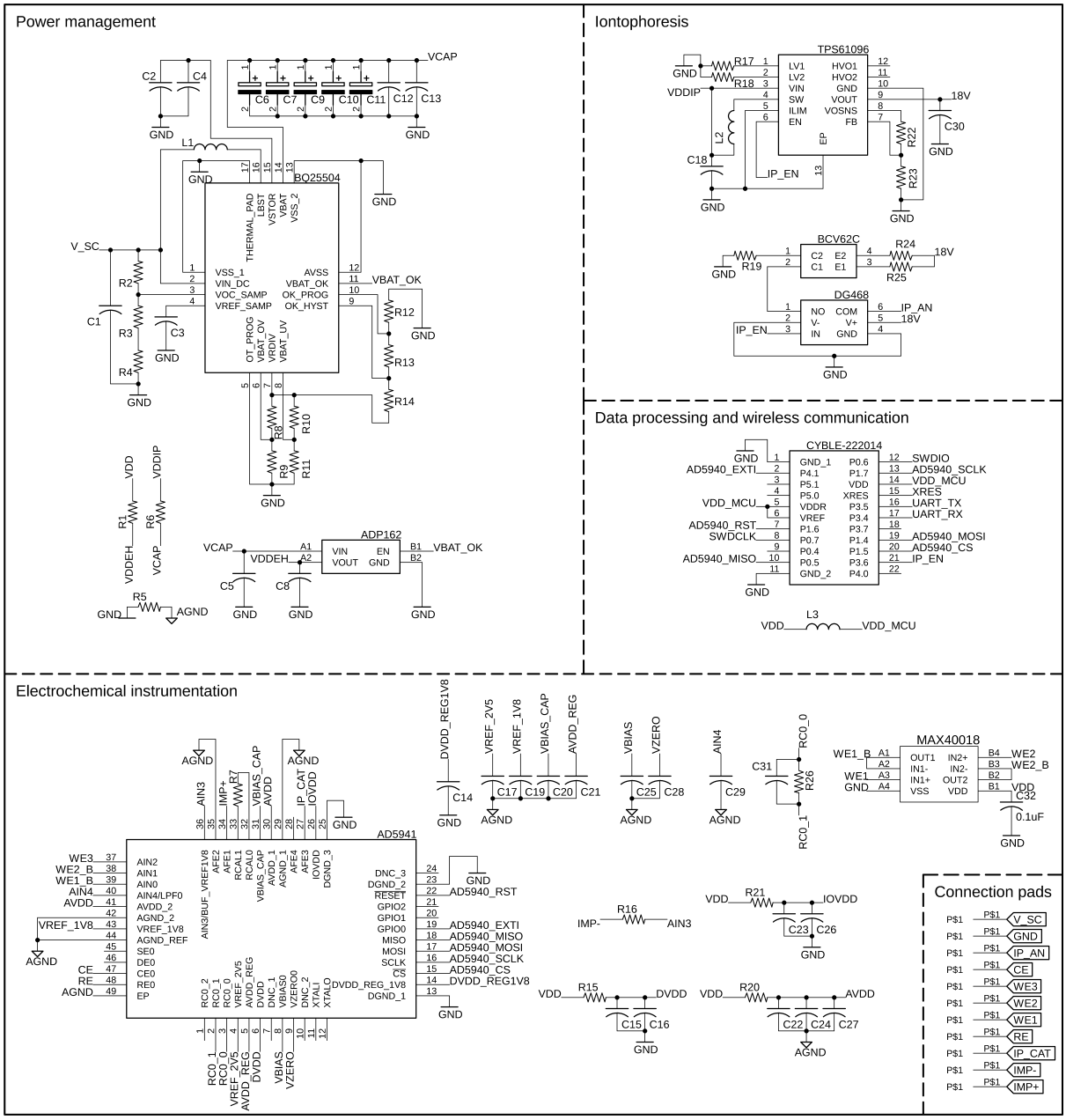

Supplementary Figure 15. Circuit schematic of the wearable electronic system. Schematic is divided into 4 main blocks for: power management, iontophoresis, data processing and wireless communication, and electrochemical instrumentation.

Discrete Components	Value	Package
R1, R5, R6, R16, R21	0 Ω	R0201
R2	3.4 MΩ	R0402
R3	10 MΩ	R0201
R4	6.65 MΩ	R0402
R7	470 Ω	R0201
R8, R11	6.2 MΩ	R0201
R9, R10, R13	3.6 MΩ	R0201
R12	2.49 MΩ	R0201
R14	3.9 MΩ	R0201
R15, R20	2.2 Ω	R0201
R17, R18	1 MΩ	R0201
R19, R24, R25	300 kΩ	R0201
R22	169 kΩ	R0201
R23	10 kΩ	R0201
R26	1.5 MΩ	R0201
C1, C2	4.7 μF	C0201
C3, C4	0.1 μF	C0201
C5, C8	1 μF	C0201
C6, C7, C9, C10, C11	1 mF	C2812
C12, C18, C19	4.7 μF	C0201
C13, C16, C24, C25, C26, C27, C29, C31, C32	0.1 μF	C0201
C14, C17, C20, C21	0.47 μF	C0201
C15, C22, C23	10 μF	C0402
C28	1 μF	C0201
C30	10 μF	C0603

Supplementary Figure 16. List of discrete components used in the wearable electronic system.

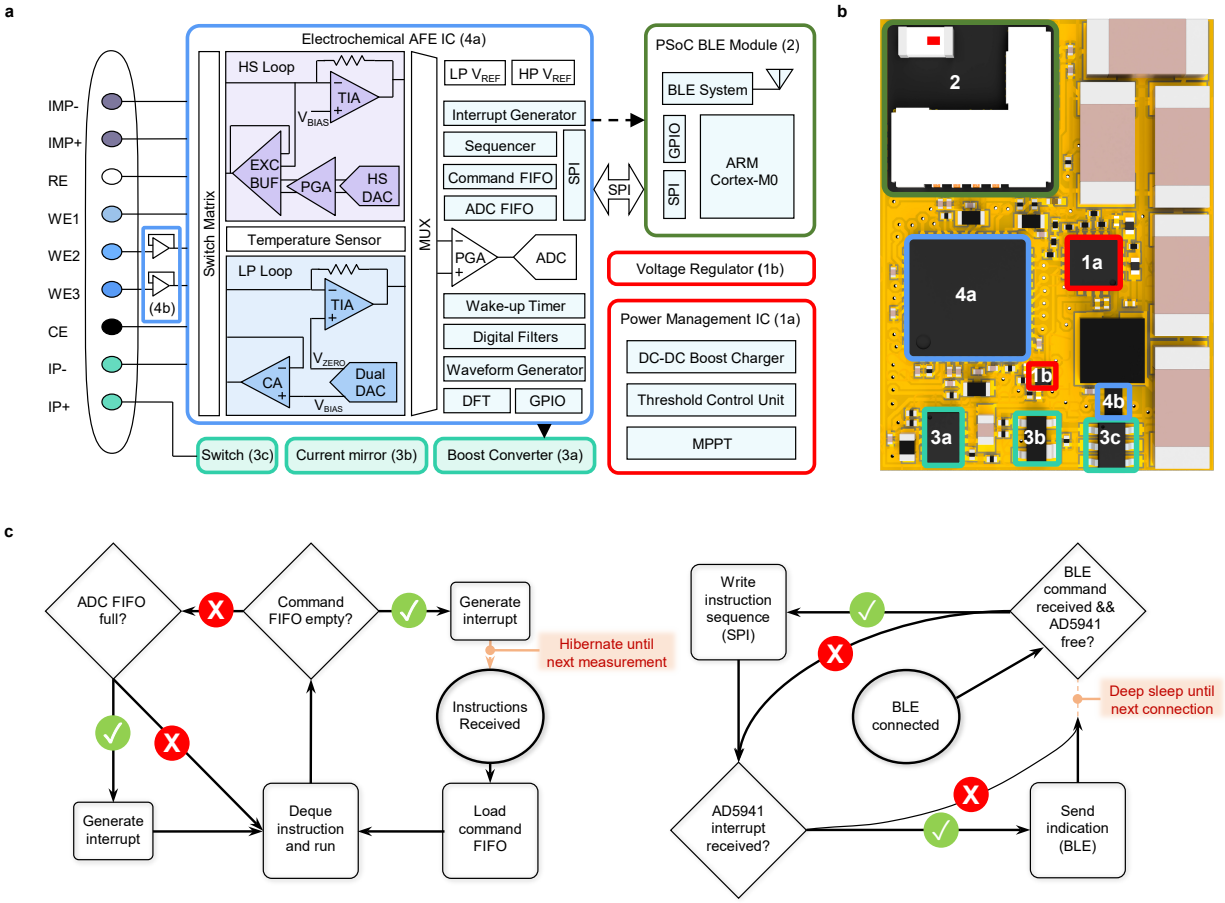

Supplementary Figure 17. Electronic system design. a, A detailed block diagram of the wearable device numerically labeled according to functional blocks: (1) power management, (2) data processing and wireless communication, (3) iontophoresis, and (4) electrochemical instrumentation. TIA, transimpedance amplifier; EXC BUF, excitation buffer; PGA, programmable gain amplifier; DAC, digital to analog converter; CA, control amplifier; HP, high power; FIFO, first in first out; DFT, discrete Fourier transform; GPIO, general purpose input output; DC, direct current; MPPT, maximum power point tracking. **b,** Top view of the FPCB with major components numerically labeled according to their function. **c,** Flow diagram of the low power embedded system algorithm composed of the electrochemical AFE (left) and PSoC BLE module (right).

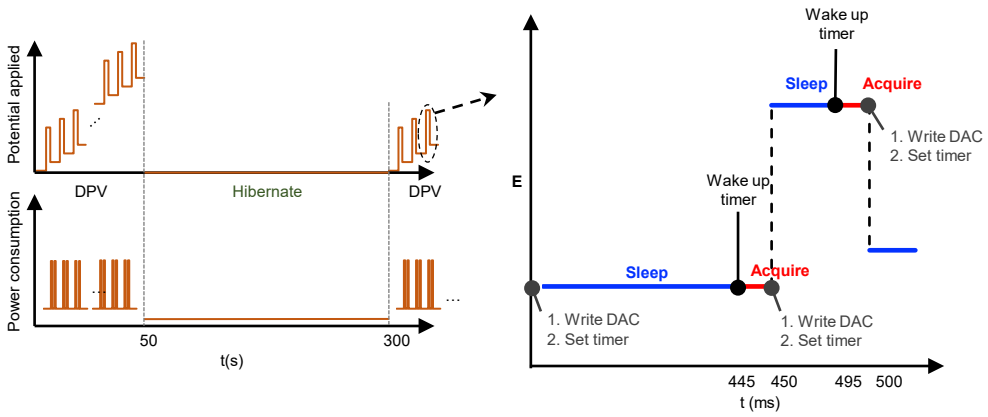

Supplementary Figure 18. Illustration showing how the electrochemical AFE operates during a DPV measurement. During DPV, the AFE applies a dynamic pulsed staircase waveform across the electrochemical cell and briefly samples the current periodically. In each step of the staircase waveform, the AFE sets the DAC to apply a baseline potential, sets the timer such that the AFE can sleep for a specified duration (pulse period – pulse width – acquire period), then acquires current data once woken up. Next, the AFE sets the DAC to apply a pulsed potential (baseline potential + pulsed amplitude), sets the timer such that the AFE can sleep for a specified duration (pulse width – acquire period), then acquires current data once woken up. After this cycle, the AFE sets the DAC to apply the new baseline potential (baseline potential + step potential) and repeats the cycle until the end of the measurement.

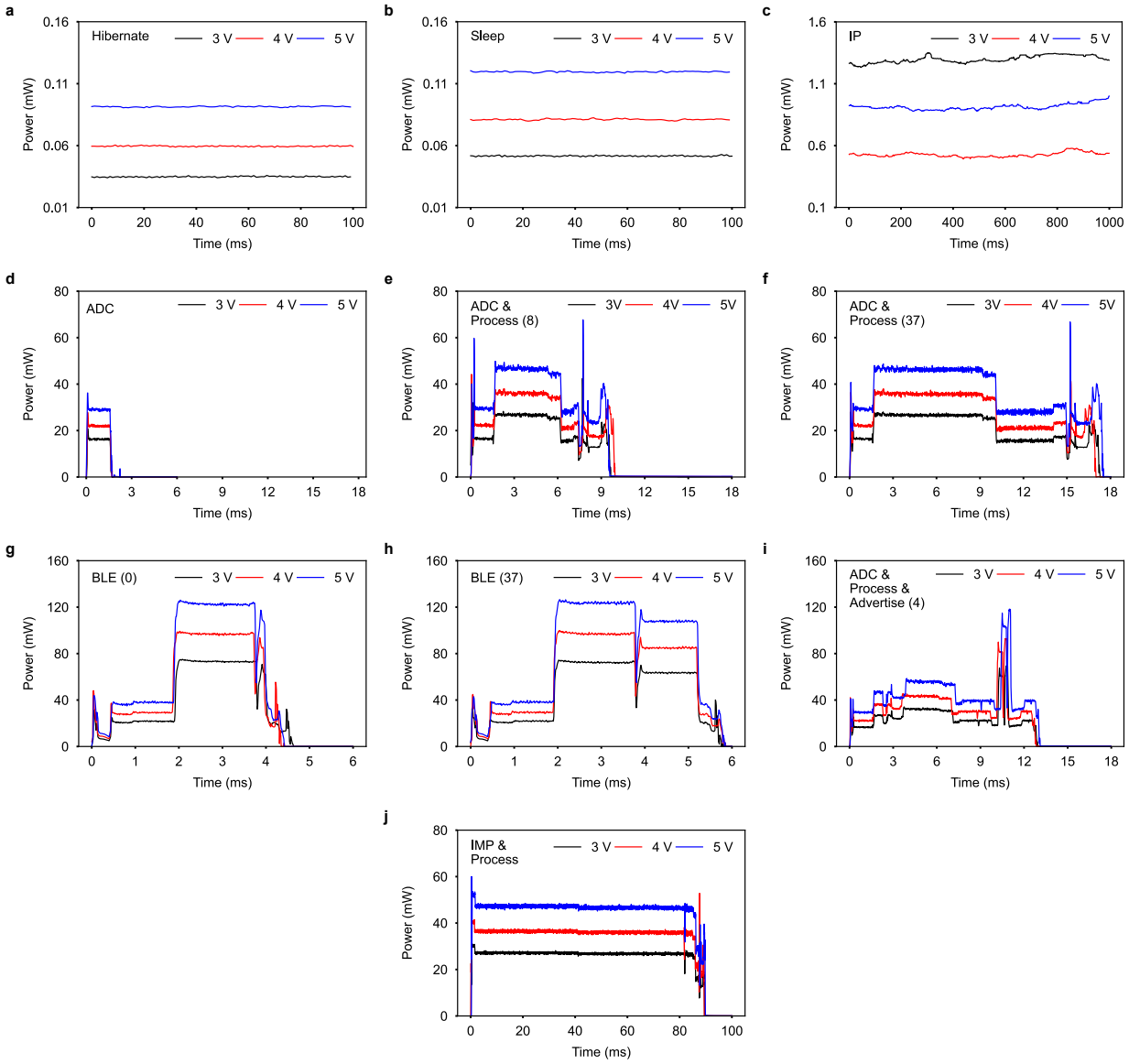

Supplementary Figure 19. Instantaneous power consumption of the electronic system while performing various tasks while powered under varying supply voltages. a–j, The performed tasks include: hibernation (**a**), sleep (**b**), iontophoresis (**c**), an ADC measurement (**d**), an ADC measurement followed by the processing of 8 and 37 measurement data sets (**e,f**), a BLE connection event with no measurement data and 37 measurement data to transmit (**g,h**), an ADC measurement followed by the processing and transmission (BLE advertisement) of 4 measurement data (**i**), and the acquisition and processing of an impedance measurement (**j**).

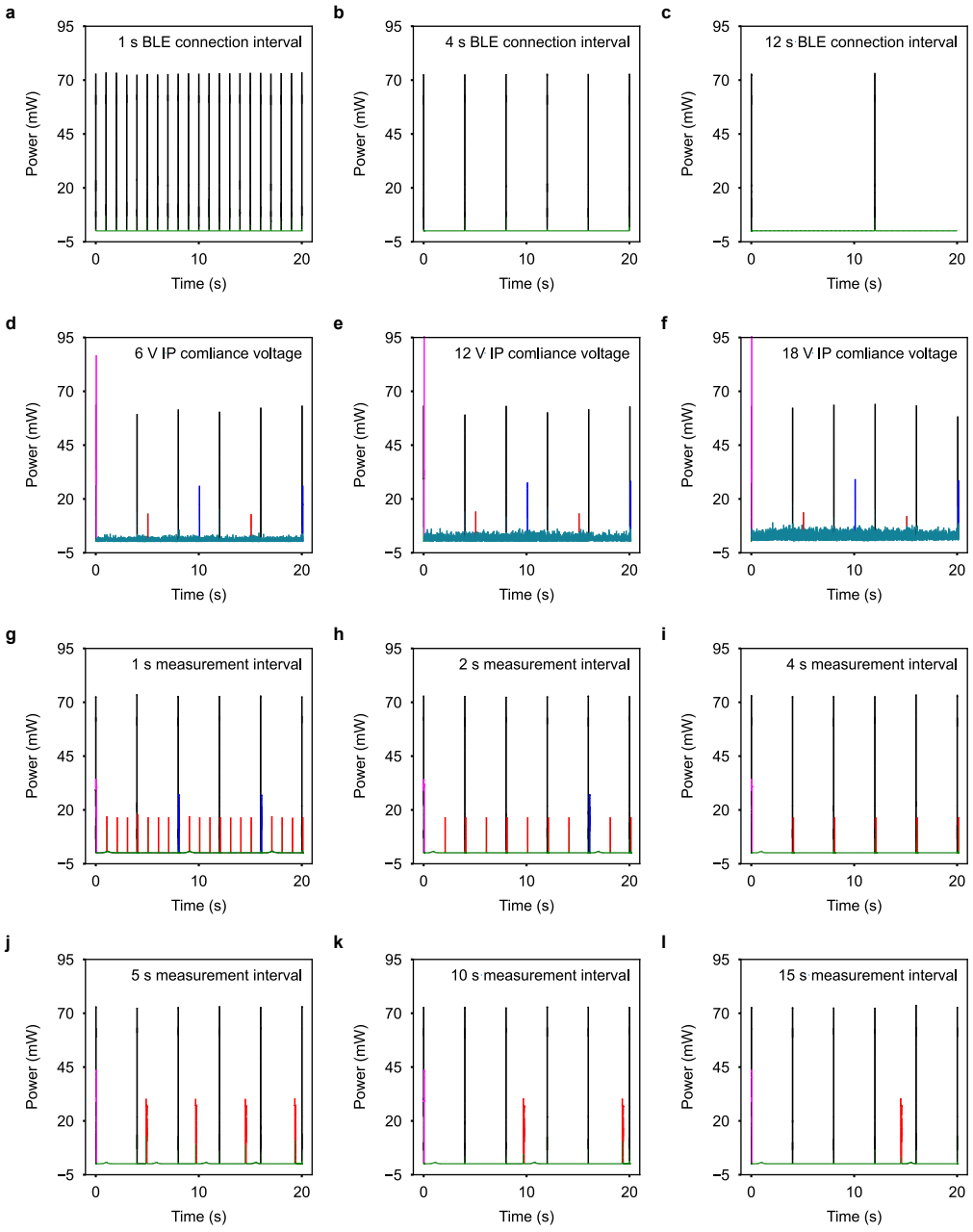

Supplementary Figure 20. Power consumption of electronic system supplied at 3 V when performing various operations under varying operation parameters. a–l, Operations include: standby with a 1 s (**a**), 4 s (**b**), and 12 s (**c**) BLE connection interval; current monitored iontophoresis with a compliance voltage of 6 V (**d**), 12 V (**e**), and 18 V (**f**); multiplexed measurements (1 amperometric, 2 potentiometric, 1 temperature) with a ADC interval of 1 s (**g**), 2 s (**h**), and 4 s (**i**); and impedance measurements with a measurement interval of 5 s (**j**), 10 s (**k**), and 15 s (**l**).

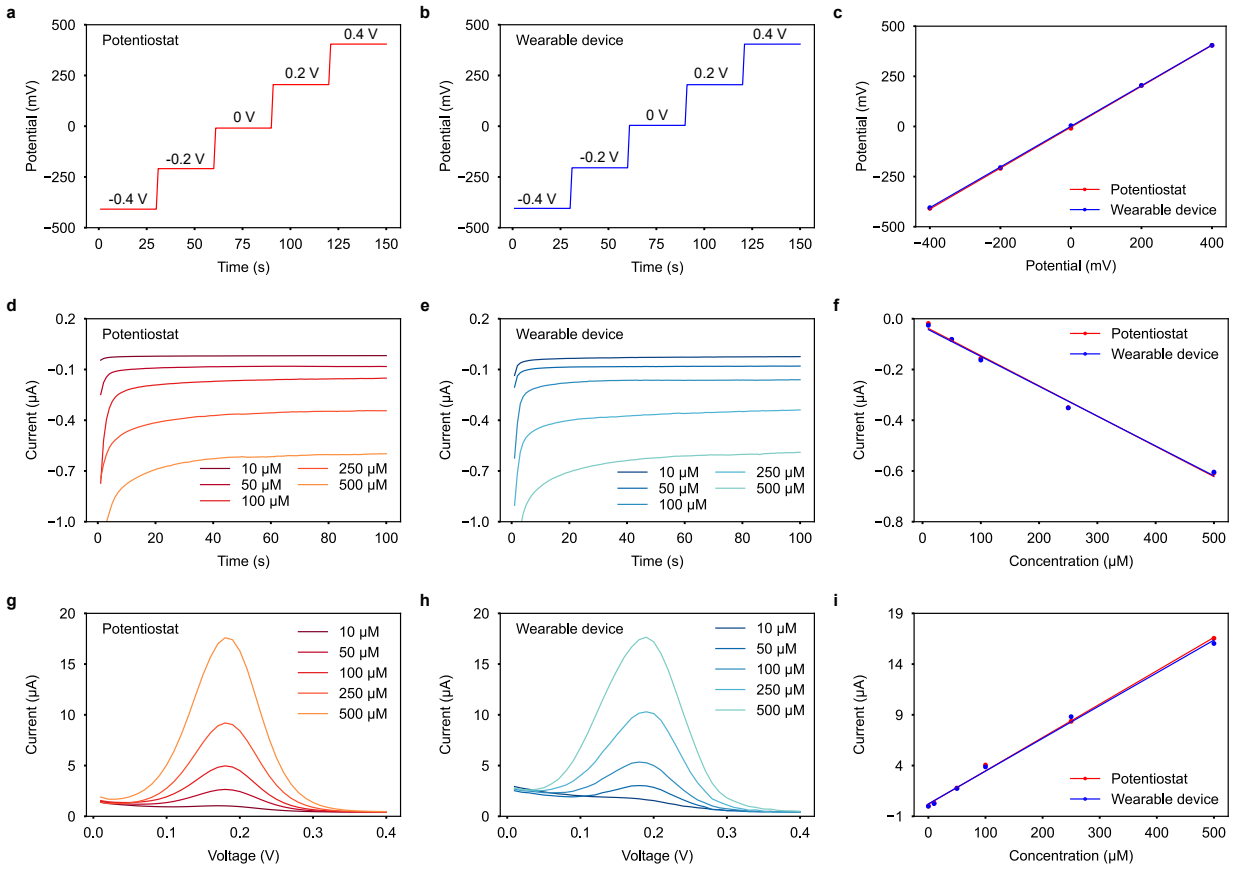

Supplementary Figure 21. Validation of the wearable device for electrochemical measurements. a–c, OCP response (1 s sampling interval) to power supply produced voltage signals recorded by a benchtop potentiostat (**a**), and by the wearable device (**b**), and their overlayed calibration curves (**c**). **d-f**, Chronoamperometric response (1 s sampling interval) to a hydrogen peroxide solution (10–500 µM H_2O_2 in 1x PBS) on a Prussian blue modified carbon electrode recorded by a benchtop potentiostat (**d**), and by the wearable device (**e**), and their overlayed calibration curves (**f**). **g-i**, DPV response (500 ms pulse period, 50 ms pulse width, 10 mV step potential, 50 mV pulse amplitude) to ferricyanide solutions (10–500 µM $K_3Fe(CN)_6$ in 0.2 M KCl) on an LEG recorded by a benchtop potentiostat (**g**), and by the wearable device (**h**), and their overlayed calibration curves of the oxidation peak current heights (**i**).

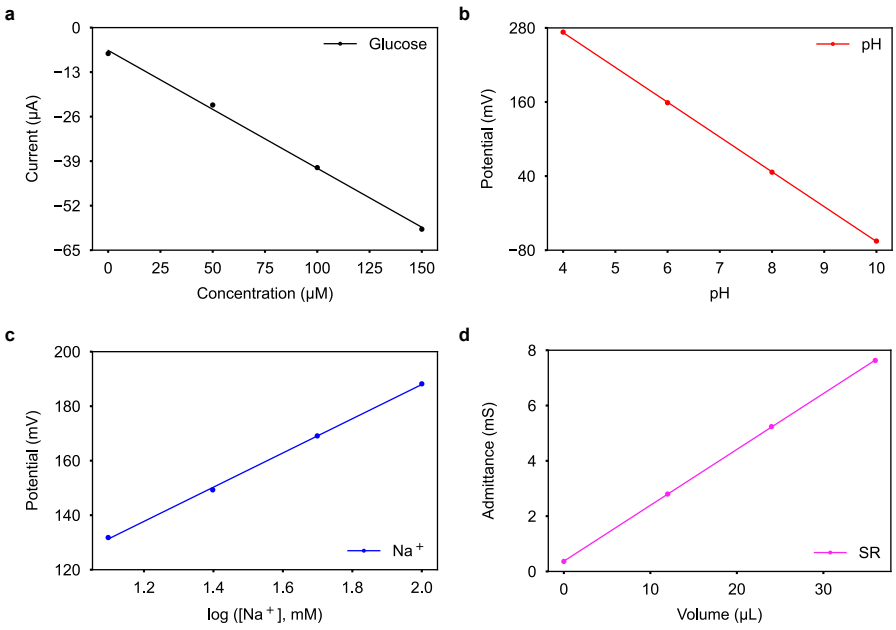

Supplementary Figure 22. Calibration plots of biosensors in physiological biomarker levels. Characterized sensors include: the glucose sensor (**a**), pH sensor (**b**), Na^+ sensor (**c**), and sweat rate (SR) sensor (**d**).

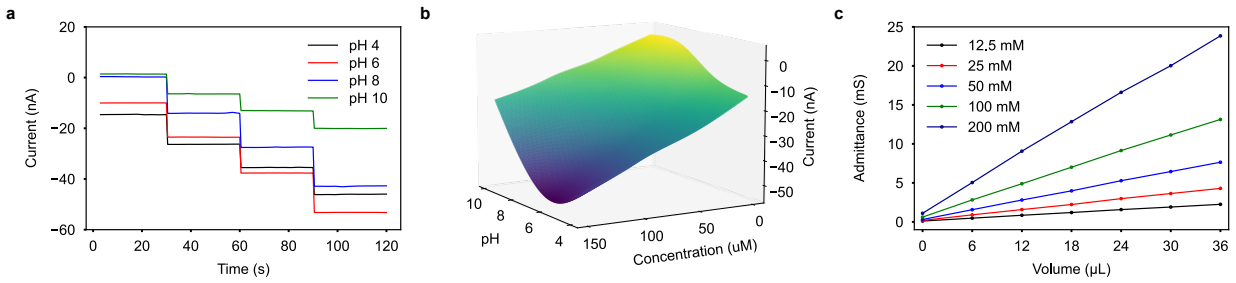

Supplementary Figure 23. Dependence of the glucose sensor on pH, and the sweat rate sensor on Na^+. a,**b**, Current response of the glucose sensor in 0–150 µM glucose with varying pH levels (**a**), and the corresponding 3D calibration plot (**b**). **c**, Admittance response of the sweat rate sensor while NaCl solutions fill up the sweat rate sensor reservoir.

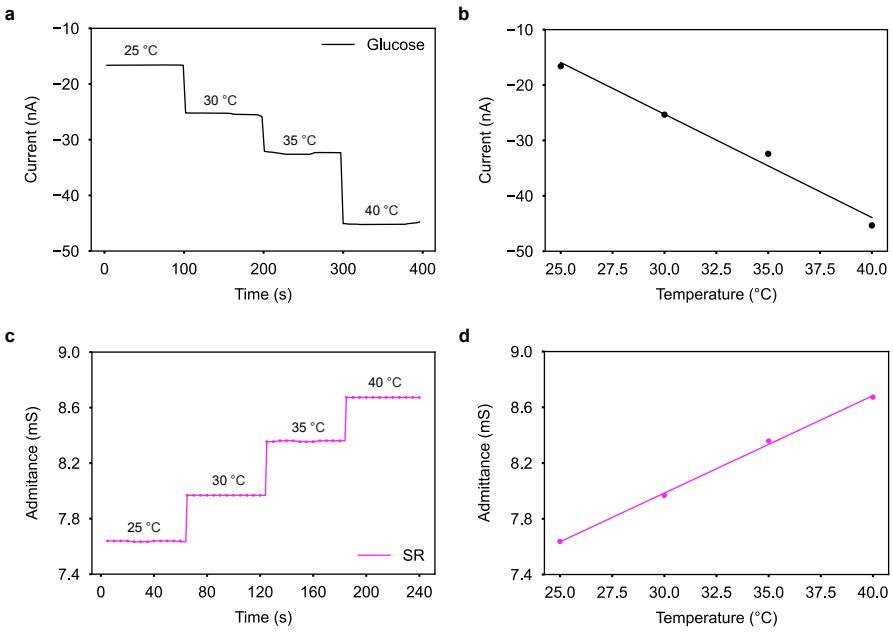

Supplementary Figure 24. Dependence of sensors on temperature. a,**b**, Glucose sensor response (50 μM glucose) under varying temperatures (**a**) and the corresponding calibration plot (**b**). **c**,**d**, Sweat rate sensor response under varying temperatures (**c**) and the corresponding calibration plot (**d**).

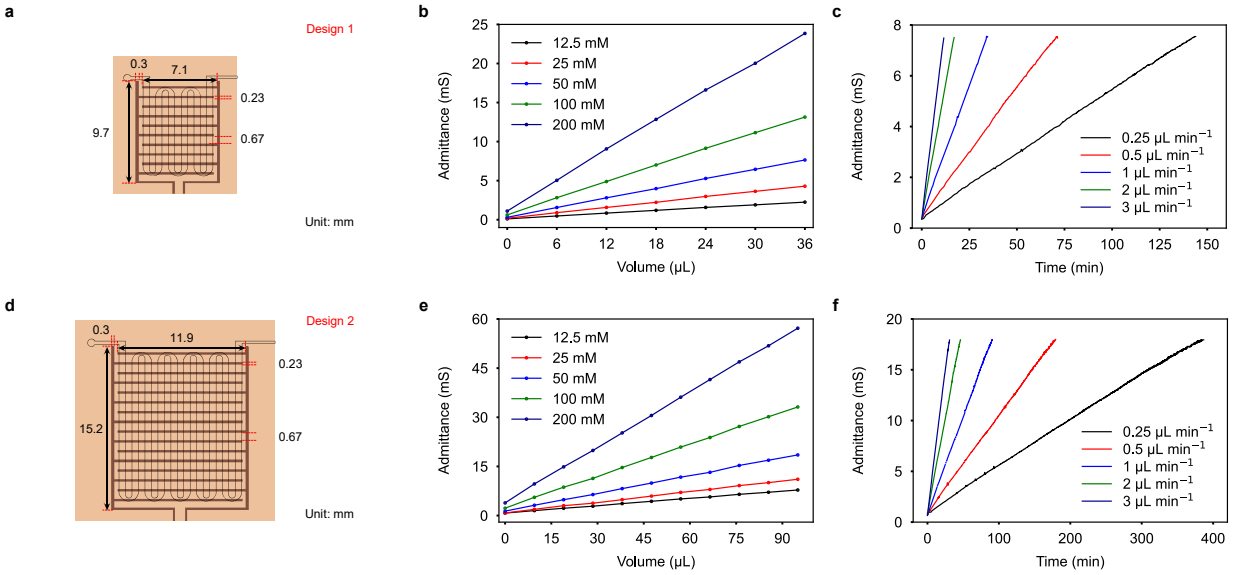

Supplementary Figure 25. Characterization of sweat rate sensors with different volumetric capacities. a,**b**, Schematic of the microfluidic sweat rate sensor with a 36 μL volumetric capacity (**a**), and the admittance response of the sweat rate sensor measured by the wearable device as NaCl solutions (12.5 mM ~ 200 mM NaCl in DI) fill up the reservoir (**b**). **c**, Response of the sweat rate sensor measured by the wearable device while a 50 mM NaCl solution fills the reservoir at varying flow rates. **d–f**, Repeated characterization for microfluidic sweat rate sensor with a 96 μL volumetric capacity.

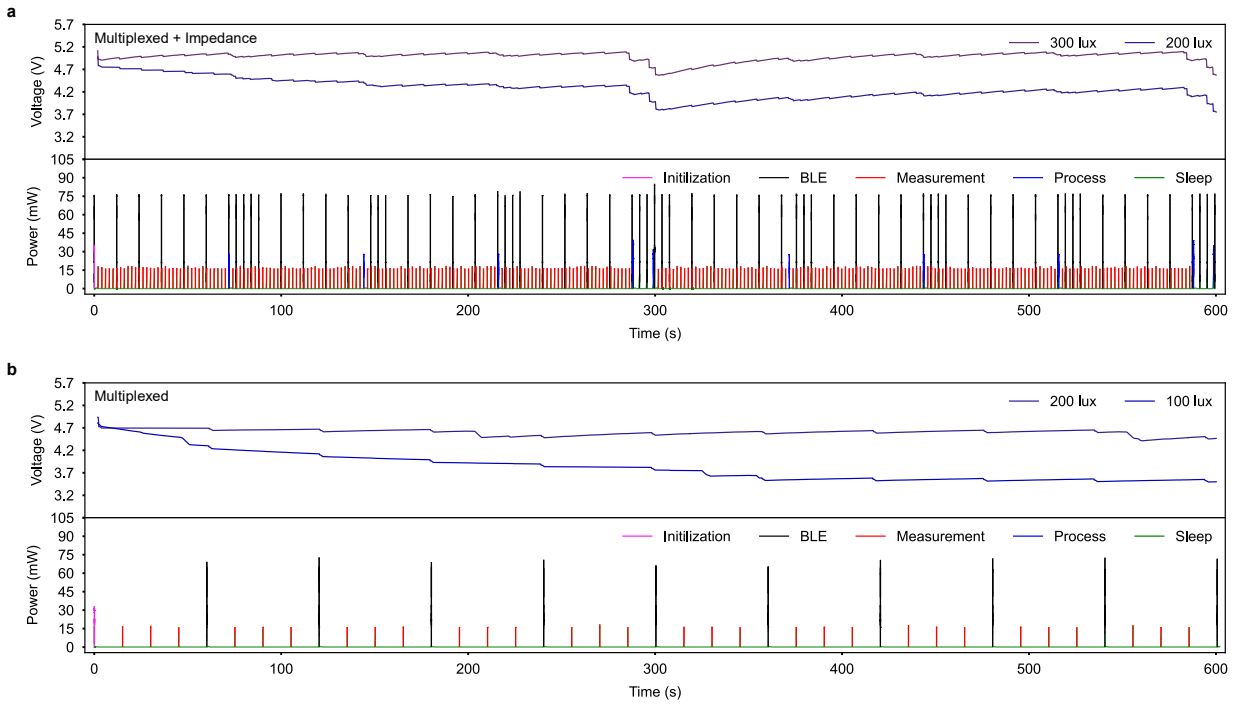

Supplementary Figure 26. Characterization of the wearable device performing multiplexed on-body measurement sequences while powered by a commercial flexible solar cell (8.9 cm x 7.4 cm) under dark indoor light intensities. a, Expanded view of power consumption profile of multiplexed measurements with a 2 s interval (8 s per data set), impedance measurements with a 5 min interval, and BLE connection with a connection interval of 4 s and a slave latency of 8 s (bottom); corresponding capacitor charging-discharging curve when powered at 300 and 200 lx by a LED (top). **b**, Expanded view of power consumption profile of multiplexed measurements with a 15 s interval (60 s per data set), and BLE advertisements with a transmission interval of 60 s (bottom); corresponding capacitor charging-discharging curve when powered at 200 and 100 lux by a LED (top).

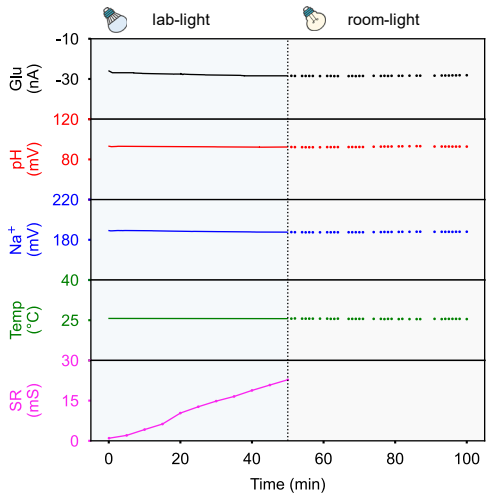

Supplementary Figure 27. In vitro multimodal monitoring of biomarkers in a glucose solution (100 µM glucose in pH 7.4 PBS) with a constant flow rate of 1 µL min^{-1}. The wearable device was powered by lab-light (1200 lx) for the first 50 minutes, and powered by room-light (600 lx) for the next 50 minutes.

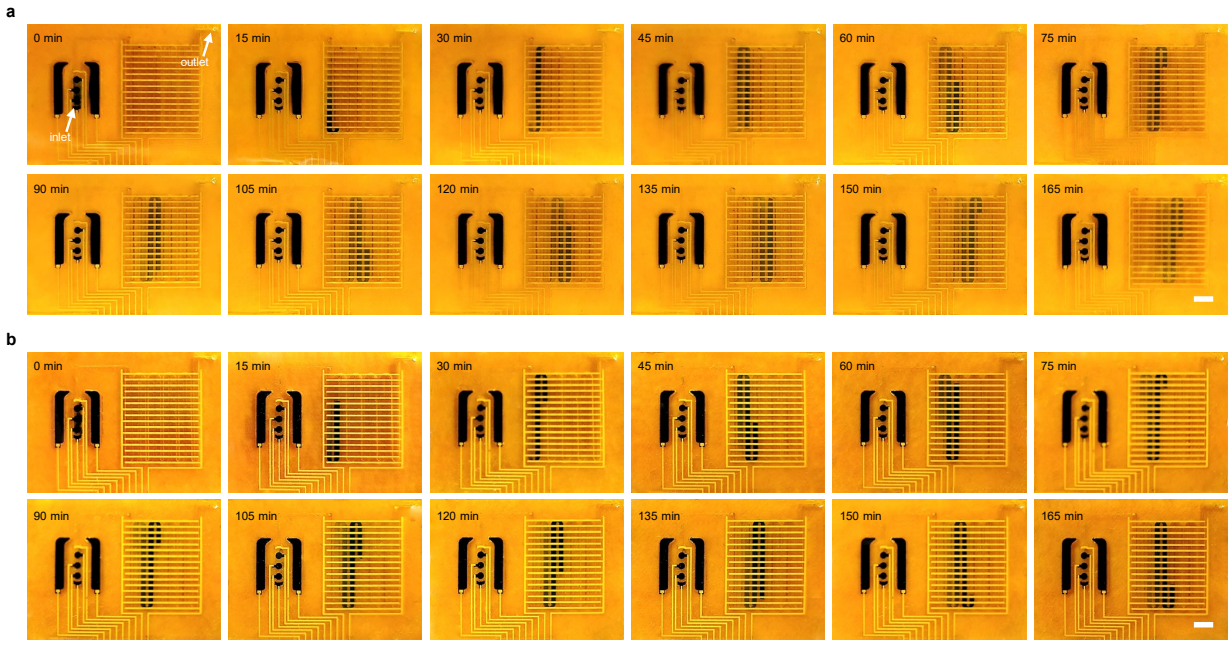

Supplementary Figure 28. On-body evaluation of the wearable device's light-powered iontophoresis and sweat processing system at rest. a,b, Time-lapsed photos in minutes after 10 minutes of iontophoresis under bright laboratory light for two subjects. Blue dye was placed on the sweat accumulation layer to visualize the sweat filling the biosensor and sweat rate sensor reservoirs at rest. Scale bars, 3 mm.

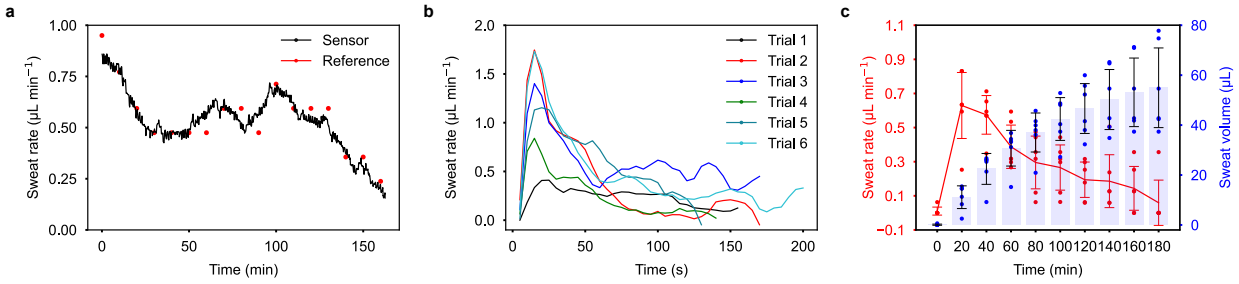

Supplementary Figure 29. On-body evaluations of the wearable device's iontophoresis and sweat rate monitoring system at rest. a, Iontophoresis induced on-body sweat rate sensor measurement with a 5 s impedance measurement interval validated by visually measured sweat rate. **b**, Iontophoresis induced sweat rate sensor responses from 6 subjects. **c**, Average iontophoresis induced sweat rates and accumulated sweat volumes and over 3 hours. Data are presented as mean ± SD (n = 6 subjects).

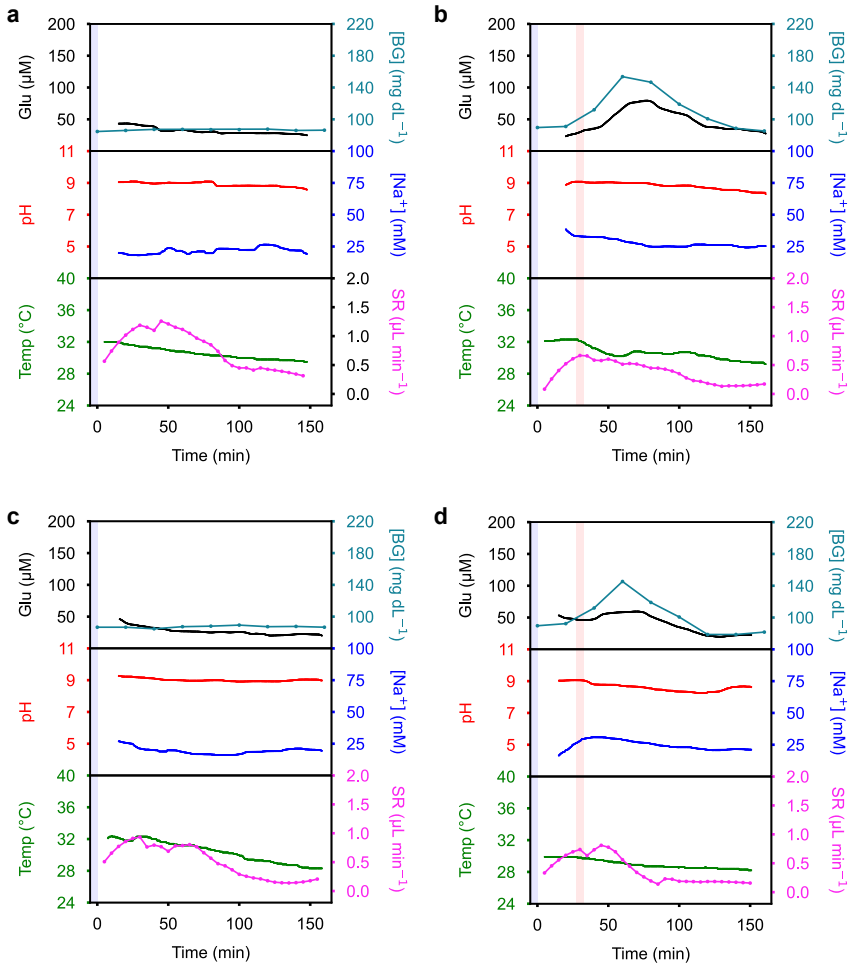

Supplementary Figure 30. Evaluation of the wearable device for multiplexed physiological monitoring in Subject 2. a,b, Wearable device-enabled autonomous multiplexed physiological monitoring at a fasting state (**a**) and after a glucose tolerance test (**b**) under lab-light illumination. **c**,**d**, Wearable device-enabled autonomous multiplexed physiological monitoring repeated on subject 2.

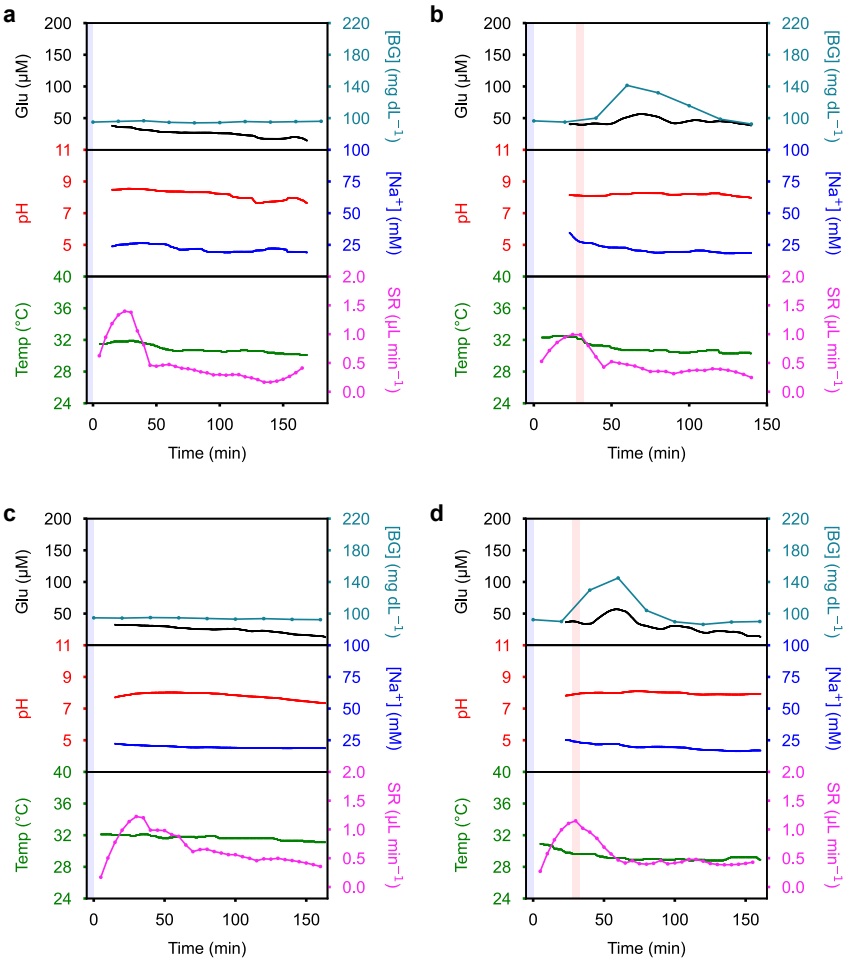

Supplementary Figure 31. Evaluation of the wearable device for multiplexed physiological monitoring in Subject 3. a,b, Wearable device-enabled autonomous multiplexed physiological monitoring at a fasting state (**a**) and after a glucose tolerance test (**b**) under lab-light illumination. **c**,**d**, Wearable device-enabled autonomous multiplexed physiological monitoring repeated on subject 3.

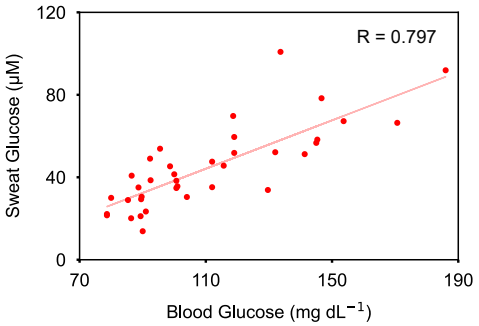

Supplementary Figure 32. Correlation between blood glucose levels and sweat glucose levels measured during sedentary glucose tolerance tests across 3 subjects.

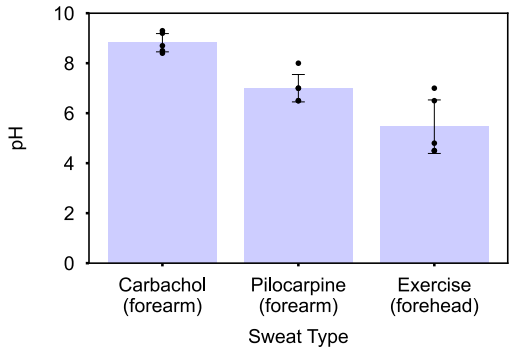

Supplementary Figure 33. Relationship between the sweat induction location/method and sweat pH. Data are presented as mean ± SD (n = 5 subjects).

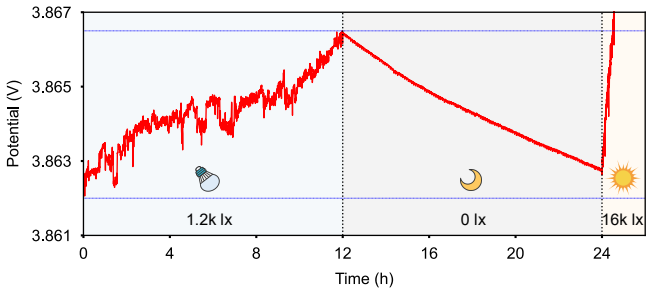

Supplementary Figure 34. Operation of battery-aided wearable device for over 24 hours while exposed to various illumination conditions. The potential of the 3.7 V battery was continuously monitored while the wearable device performed multiplexed measurement sequences.

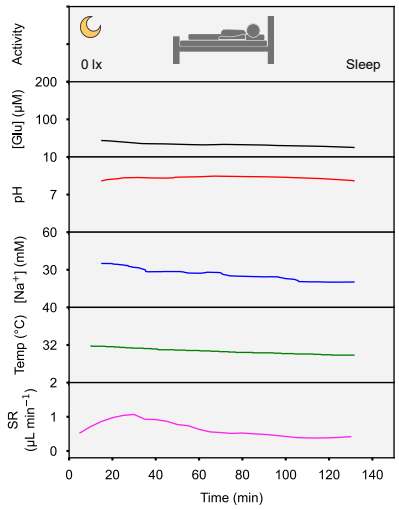

Supplementary Figure 35. Evaluation of the light-powered wearable device for physiological monitoring during sleep without the access to light. A 3.7 V battery was integrated into the wearable system and charged during the day with available ambient light.

Supplementary Table 1. FPSC performance under full sunlight conditions. Average solar cell performance parameters extracted from JV curves recorded under simulated sunlight illumination (AM1.5G) (mean ± SD, n = 7), with the best performance shown in square brackets. Pixel size "small" corresponds to 0.165 cm^2, "large" to 1 cm^2, and "module" to 2 individual 1cm^2 cells connected in series.

Pixel size	**Scan direction**	**V_{oc}** (V)	**J_{sc}** (mA cm^{-2})	**FF** (%)	**PCE** (%)
small	Forward	1.102±0.005 [1.107]	20.1±1.3 [21.4]	74.2±0.5 [74.8]	16.4±1.3 [17.7]
small	Reverse	1.106±0.008 [1.115]	20.2±1.3 [21.7]	74.3±0.5 [75.0]	16.6±1.5 [18.1]
large	Forward	1.075±0.028 [1.107]	20.0±0.5 [20.6]	66.9±0.6 [67.6]	14.7±0.7 [15.4]
large	Reverse	1.081±0.024 [1.109]	20.1±0.5 [20.5]	71.8±0.7 [72.5]	15.6±0.7 [16.5]
module	Forward	2.149±0.060 [2.237]	8.8±0.2 [9.0]	64.9±0.7 [65.6]	12.3±0.7 [13.3]
module	Reverse	2.184±0.056 [2.241]	8.8±0.2 [9.1]	67.8±0.7 [68.5]	13.1±0.6 [14.0]

Supplementary Table 2. FPSC performance under LED illumination. Photovoltaic parameters extracted from JV curves recorded under 600 lx (215 μW cm^{-2}) indoor illumination using a white light LED, 2700 K (mean ± SD, n = 7), with the best performance shown in square brackets. Pixel size "small" corresponds to 0.165 cm^2, "large" to 1 cm^2, and "module" to 2 individual 1cm^2 cells connected in series.

Pixel size	**Scan direction**	**V_{oc}** (V)	**J_{sc}** (μA cm^{-2})	**FF (%)**	**P_{max}** (μW cm^{-2})	**PCE** (%)
small	Forward	0.929±0.003 [0.936]	87.28±0.06 [87.35]	79.9±0.8 [80.8]	64.8±1.2 [66.1]	30.1±0.5 [30.8]
small	Reverse	0.940±0.004 [0.948]	88.11 ±0.06 [88.11]	79.3±0.8 [80.2]	65.7±1.2 [67.1]	30.6±0.5 [31.2]
large	Forward	0.918±0.007 [0.936]	85.82±0.04 [85.87]	76.6±0.9 [77.6]	60.4±1.3 [61.8]	28.1±0.6 [28.7]
large	Reverse	0.935±0.006 [1.853]	86.03±0.03 [86.07]	78.0±0.9 [78.9]	62.9±1.2 [64.2]	29.2±0.5 [29.9]
module	Forward	1.842±0.009 [1.853]	47.70±0.02 [43.76]	75.1±1.0 [76.2]	60.5±1.2 [61.8]	28.1±0.6 [28.7]
module	Reverse	1.857 ±0.007 [1.866]	43.92±0.03 [43.96]	76.7±1.0 [77.7]	62.5±1.2 [63.7]	29.1±0.6 [29.6]

Supplementary Table 3. List of the best performing indoor flexible solar cells among different PV technologies. a-Si – amorphous silicon, III-V - , CIGS - , DSSC – dye sensitized solar cells, OPV – organic photovoltaics, PVSK – perovskite solar cells[8–14].

Material	**Light source**	**Illuminance** (lx)	**PCE** (%)	**Reference**
a-Si	Fluorescent	300	8.7	[8]
III-V	Fluorescent	1000	21	[9]
CIGS	Incadescent	3000	5.3	[10]
OPV	Fluorescent	800	13.5	[11]
DSSC	Fluorescent	1000	28.9	[9]
PVSK	LED	400	22.6	[12]
PVSK	LED 6400K	400	23.3	[13]
PVSK	LED 6400K	600	25.3	[13]
PVSK	LED 6400K	1000	25.7	[13]
PVSK	LED 2700K	400	13.3	[14]
PVSK	LED 6400K	600	31.2	This work

Supplementary Table 4. Performance of quasi-2D FPSC under laser illumination. Photovoltaic parameters extracted from selected JV curves recorded under monochromatic laser light (λ = 637 nm), with values recorded at AM1.5 and 600 lx LED 2700K included for comparison. Pixel size "small" corresponds to 0.165 cm^2, "large" to 1 cm^2, and "module" to 2 individual 1cm^2 cells connected in series. R_s and R_p values were calculated from slope near V_{oc} and J_{sc} respectively.

Pixel size	**Light source**	**V_{oc}** (V)	**J_{sc}** (mA cm^{-2})	**FF** (%)	**PCE** (%)	**R_s** (Ω cm^2)	**R_p** (kΩ cm^2)
small	AM1.5	1.115	21.7	75.0	18.1	4.5	3.9
	Laser (12.23 mW cm^{-2})	1.102	5.7	80.9	41.3	15	28
	Laser (5.43 mW cm^{-2})	1.074	2.5	82.5	40.2	29	124
	Laser (0.194 mW cm^{-2})	0.947	0.070	82.6	34.5	383	535
	LED 600lx (0.215 mW cm^{-2})	0.948	0.088	80.2	31.2	306	500
large	AM1.5	1.109	20.5	72.5	16.5	8.3	7.5
	Laser (12.23 mW cm^{-2})	1.080	4.7	73.7	29.4	25	126
	Laser (5.43 mW cm^{-2})	1.050	2.3	76.0	30.4	34	259
	Laser (0.286 mW cm^{-2})	0.948	0.108	79.3	28.4	329	390
	LED 600lx (0.215 mW cm^{-2})	0.945	0.086	78.9	29.9	389	437
module	AM1.5	2.241	9.1	68.5	14.0	21.1	10.7
	LED 600lx (0.215 mW cm^{-2})	1.866	0.044	77.7	29.6	1014	795

Supplementary Table 5. Average power consumption of electronic system supplied at 3 V while performing various operations under varying operation parameters. Blocks highlighted in yellow represent average power consumptions of power consumption profiles shown in **Fig. 3d**, and blocks highlighted in green represent average power consumptions of power consumption profiles shown in **Fig. 3f**.

Operation	Operation parameters		Power consumption (µW)
Standby	BLE connection interval	1 s	127
		4 s	82
		12 s	72
Iontophoresis	Compliance voltage	6 V	719
		12 V	1604
		18 V	2589
Potentiometry	Measurement interval	1 s	147
		2 s	119
		4 s	103
Amperometry	Measurement interval	1 s	161
		2 s	129
		4 s	111
Differential pulse voltammetry	Pulse period	0.25 s	334
		0.5 s	211
		1 s	142
Impedance analysis	Measurement interval	5 s	600
		10 s	343
		15 s	252
Multiplexed measurement (1 amperometry, 2 potentiometry, 1 temperature)	Measurement interval	1 s	170
		2 s	132
		4 s	110
On-body measurement sequence	Multiplexed (1 s interval) + impedance (5 min interval) + BLE connection (4 s interval)		203
	Multiplexed (2 s interval) + impedance (5 min interval) + BLE connection (4 s interval with slave latency of 2)		129
	Multiplexed (15 s interval) + BLE advertisement (60 s interval)		58

Supplementary References

1. Steim, R. *et al.* Organic photovoltaics for low light applications. *Sol. Energy Mater Sol. Cells* **95**, 3256–3261 (2011).
2. Zheng, H. *et al.* Emerging organic/hybrid photovoltaic cells for indoor applications: Recent advances and perspectives. *Sol. RRL* **5**, 2100042 (2021).
3. Polyzoidis, C., Rogdakis, K. & Kymakis, E. Indoor perovskite photovoltaics for the internet of things—challenges and opportunities toward market uptake. *Adv. Energy Mater.* **11**, 2101854 (2021).
4. Ho, J. K. W., Yin, H. & So, S. K. From 33% to 57% – an elevated potential of efficiency limit for indoor photovoltaics. *J. Mater. Chem. A* **8**, 1717–1723 (2020).
5. Muhammad, B. T., Kar, S., Stephen, M. & Leong, W. L. Halide perovskite-based indoor photovoltaics: recent development and challenges. *Mater. Today Energy* **23**, 100907 (2022).
6. Yin, H. *et al.* Designing a ternary photovoltaic cell for indoor light harvesting with a power conversion efficiency exceeding 20%. *J. Mater. Chem. A* **6**, 8579–8585 (2018).
7. Runa, A. *et al.* Highly reproducible perovskite solar cells based on solution coating from mixed solvents. *J. Mater. Sci.* **53**, 3590–3602 (2018).
8. Foti, M. *et al.* Efficient flexible thin film silicon module on plastics for indoor energy harvesting. *Sol. Energy Mater Sol. Cells* **130**, 490–494 (2014).
9. Freitag, M. *et al.* Dye-sensitized solar cells for efficient power generation under ambient lighting. *Nat. Photon.* **11**, 372–378 (2017).
10. Sacco, A., Rolle, L., Scaltrito, L., Tresso, E. & Pirri, C. F. Characterization of photovoltaic modules for low-power indoor application. *Appl. Energy* **102**, 1295–1302 (2013).
11. Ylikunnari, M. *et al.* Flexible OPV modules for highly efficient indoor applications. *Flex. Print. Electron.* **5**, 014008 (2020).
12. Castro-Hermosa, S. *et al.* Perovskite photovoltaics on roll-to-roll coated ultra-thin glass as flexible high-efficiency indoor power generators. *Cell Rep. Phys. Sci.* **1**, 100045 (2020).
13. Kim, S. *et al.* High-power and flexible indoor solar cells via controlled growth of perovskite using a greener antisolvent. *ACS Appl. Energy Mater.* **3**, 6995–7003 (2020).
14. Dagar, J. *et al.* Efficient fully laser-patterned flexible perovskite modules and solar cells based on low-temperature solution-processed SnO_2/mesoporous-TiO_2 electron transport layers. *Nano Res.* **11**, 2669–2681 (2018).

15. Zhang, C., Zhang, J., Hao, Y., Lin, Z. & Zhu, C. A simple and efficient solar cell parameter extraction method from a single current-voltage curve. *J. Appl. Phys.* **110**, 064504 (2011).